PNAS
www.pnas.org

Supplementary Information for

An additive algorithm for origami design

Levi H. Dudte, Gary P. T. Choi, L. Mahadevan

Corresponding Author: L. Mahadevan.
E-mail: lmahadev@g.harvard.edu

This PDF file includes:

Supplementary text
Figs. S1 to S18
Legends for Movies S1 to S10
SI References

Other supplementary materials for this manuscript include the following:

Movies S1 to S10

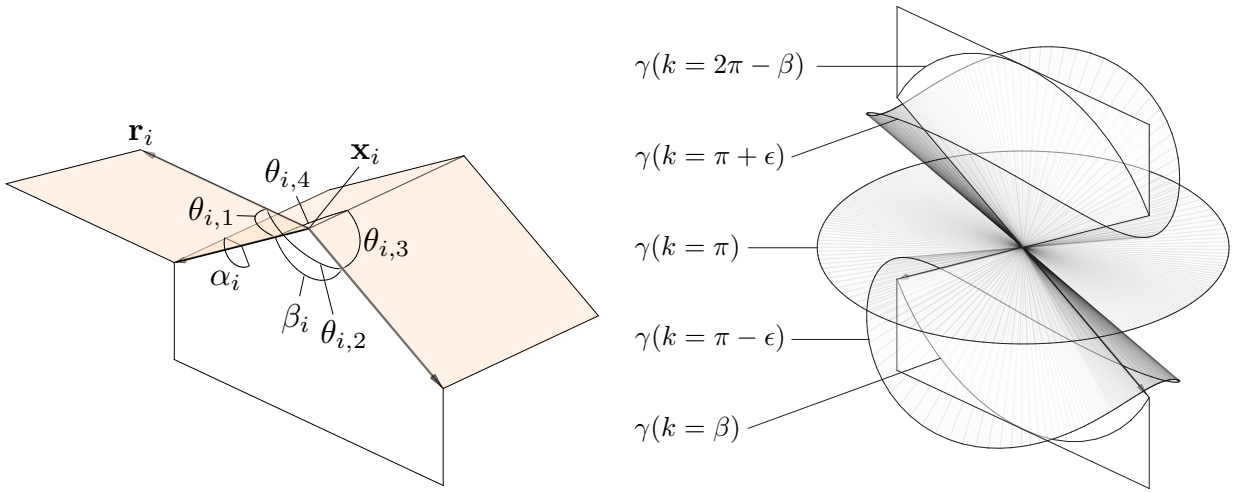

Fig. S1. Geometry of a single vertex. (Left) The angles $\theta_3 \in [0, \pi]$ and $\theta_4 \in [0, \pi]$ are preexisting design angles at the vertex $\mathbf{x}$. The angle $\beta \in [0, \pi]$ is the angle between the two boundary edges incident to $\mathbf{x}$ and defines a plane. The *flap angle* $\alpha \in [0, 2\pi]$ is the angle between the β plane and the plane of $\mathbf{r}$ and θ_1, which will be a new edge direction and a new design angle incident to $\mathbf{x}$, respectively. The angle $\theta_2 \in [0, \pi]$ is the other new design angle at $\mathbf{x}$. To analyze the geometry of this system, we consider θ_1 an independent variable sweeping through $[0, \pi]$ in the plane determined by α and θ_2 a function of θ_1, i.e. $\theta_2 = \theta_2(\theta_1)$. **(Right)** Solutions to Eq. (S1) form $\gamma(\beta, k)$ (where $k = 2\pi - \theta_3 - \theta_4$) curves, which are ellipses of spherical arcs and thus represent directions of $\mathbf{r}$ that use the exact amount of material required at this vertex to satisfy developability. These simple loops enclose the lines containing the two growth front edges at this vertex and sweeping α through $[0, 2\pi)$ uniquely selects uniquely a point on a given γ curve.

Supporting Information Text

S1. Construction

A. Completing a quad pair. Consider a potential single vertex origami of degree four, existing at the moment only as a pair of quads (i.e. two of its incident faces exist and two have yet to be designed, see Fig. S1). Let the new design angles incident to the vertex be θ_1 and θ_2 and the existing design angles be θ_3 and θ_4. Let the angle between edges at the growth boundary be $\beta \in [0, \pi]$ and the oriented angle between the β plane and the new face containing θ_1 be $\alpha \in [0, 2\pi)$. The new design angles θ_1 and θ_2 at the vertex must satisfy two equations:

$$\sum_{i=1}^{4} \theta_i = 2\pi, \qquad \text{[S1]}$$

$$\cos\theta_2 = \cos\theta_1 \cos\beta + \sin\theta_1 \sin\beta \cos\alpha. \qquad \text{[S2]}$$

Eq. (S1) guarantees the developability of the interior angles around the new interior node and Eq. (S2) expresses compatibility between θ_1, θ_2, α and β (see Fig. S1). Eq. (S2) is the familiar law of cosines from spherical trigonometry, with θ_1, θ_2 and β forming a spherical triangle with interior angle α opposite θ_2. Notice that this system expresses the same pair of constraints as prior optimization-based origami design studies (1), namely developability in Eq. (S1) and planarity by construction in Eq. (S2).

To show existence and uniqueness of solutions to this system, we begin by observing that the existing θ_3 and θ_4 values at x determine the value of $\theta_1 + \theta_2 = 2\pi - (\theta_3 + \theta_4) = k$ by Eq. (S1). This allows us to rewrite the system as

$$f(\theta_1) = \theta_1 + \theta_2(\theta_1) = k, \qquad \text{[S3]}$$

where $\theta_2(\theta_1) = \cos^{-1}(\cos\theta_1 \cos\beta + \sin\theta_1 \sin\beta \cos\alpha)$. Now we can make several observations about this equation. For the left-hand side, note that

- $f(0) = \beta$,
- $f(\pi) = 2\pi - \beta$,
- $f(\theta_1)$ is positive monotonic on $\theta_1 \in [0, \pi]$.

Intuitively, $\theta_2(\theta_1)$ always decreases at a smaller rate than the rate of increase of θ_1, except in the singular cases $\alpha = 0, \pi$ where the rates are equal and opposite and $f(\theta_1)$ is constant (see Section S1A.3 for details). These observations imply that $f(\theta_1)$ is bounded by $[\beta, 2\pi - \beta]$ and positive monotonic for $\theta_1 \in [0, \pi]$. Now for the right-hand side, observe that

- $k \in [\beta, 2\pi - \beta]$

because $\theta_3 + \theta_4 \in [\beta, 2\pi - \beta]$ (see Section S1A.2 for details). Taken together, these observations guarantee existence and uniqueness of solutions to Eq. (S3) and thereby Eq. (S1) and Eq. (S2).

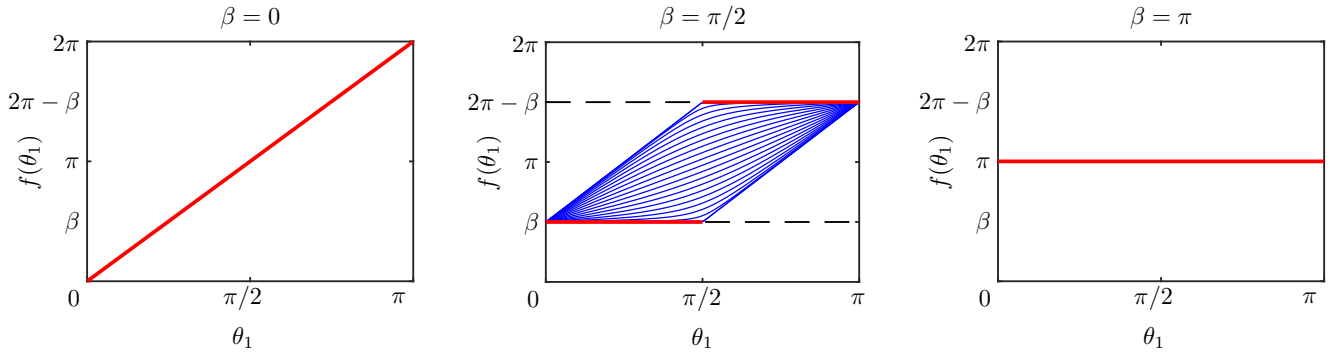

Fig. S2. Genericity vs. singularity. (Left) $\beta = 0$ (singular) The two edge vectors at this vertex are collinear and point in the same direction, so θ_2 increases at the same rate as θ_1. **(Middle)** $\beta = \pi/2$ (generic for $\alpha \neq 0, \pi$) A qualitatively general picture of S2. θ_2 decreases a smaller rate than that of the increase of θ_1, so the blue curves are positive monotonic. At $\alpha = 0, \pi$ the planes of θ_1 and θ_2 coincide with the β plane, and rates of change in θ_1 and θ_2 are either equal in magnitude with opposite sign (when $\mathbf{r}$ is inside β) or equal (when $\mathbf{r}$ is outside β). **(Right)** $\beta = \pi$ (singular) Again, the two vectors at the growth front are collinear, but now point in opposite directions, so the only possible value of $\theta_1 + \theta_2$ at this vertex is π.

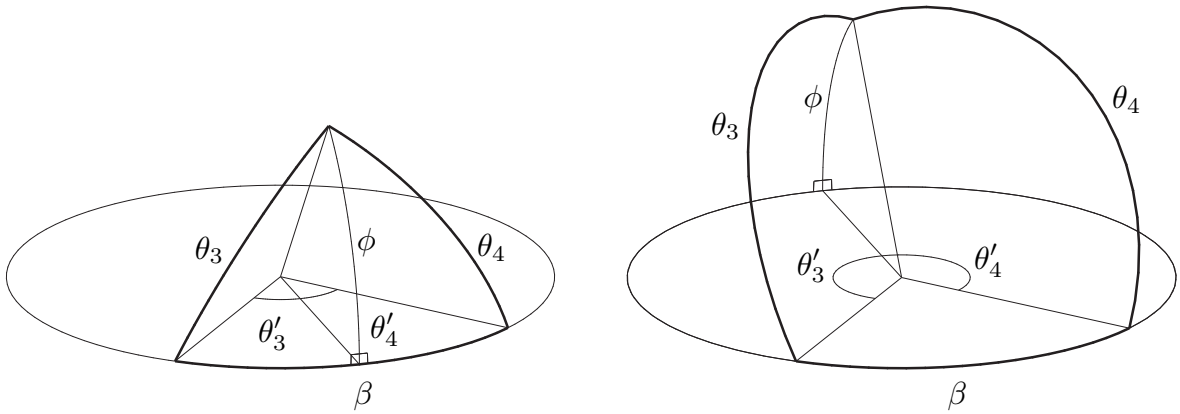

Fig. S3. Bounding the sum of two angles. Three arbitrary angles θ_3, θ_4 and β form a spherical triangle that can be divided into two spherical triangles by projecting the point between θ_3 and θ_4 to the β plane (dashed line). Denote the unsigned angle between the original point and its projection ϕ and observe that $\theta_3, \theta_4 = \pi/2$ when $\phi = \pi/2$. **(Left)** Projection onto β plane of point in $\mathbb{R}^3$ falls inside β: $\theta_3' + \theta_4' = \beta$ when $\phi = 0$. These projections can either both be less than $\pi/2$ or one less and one greater. **(Right)** Projection onto β plane of point in $\mathbb{R}^3$ falls outside β: $\theta_3' + \theta_4' = 2\pi - \beta$ when $\phi = 0$. These projections can either both be greater than $\pi/2$ or one less and one greater.

A.1. Genericity vs. singularity. In general, we will forbid singular configurations throughout this work, as these growth fronts can admit multiple solutions for a given flap angle choice. Fig. S2 illustrates the behavior of Eq. (S3) under generic ($\beta \neq 0, \pi$) and singular configurations ($\beta = 0, \pi$).

A.2. Spherical triangle inequality. Consider a spherical triangle consisting of the angles β, θ_3 and θ_4, each of which is in $[0, \pi]$. Let the angles θ_3' and θ_4' be the angles of the projections of θ_3 and θ_4, respectively, onto the plane containing β. Let ϕ be height of the node incident to θ_3 and θ_4 above the β plane (see Fig. S3).

Now consider the sum $\theta_3 + \theta_4$ for all values of ϕ. Observe that at $\phi = \pi$, $\theta_3 = \theta_4 = \pi/2$ and thus $\theta_3 + \theta_4 = \pi \in [\beta, 2\pi - \beta]\ \forall\ \beta \in (0, \pi)$. Observe also that at $\phi = 0$, there are two possibilities: $\theta_3 + \theta_4 = \beta$ (the "inside" case) and $\theta_3 + \theta_4 = 2\pi - \beta$ (the "outside" case). By projecting θ_3 and θ_4 onto the β plane, we can construct two right spherical triangles, allowing us to write

$$\cos\theta_3 = \cos\theta_3' \cos\phi + \sin\theta_3' \sin\phi \cos\frac{\pi}{2} = \cos\theta_3' \cos\phi, \qquad [S4]$$

$$\cos\theta_4 = \cos\theta_4' \cos\phi + \sin\theta_4' \sin\phi \cos\frac{\pi}{2} = \cos\theta_4' \cos\phi, \qquad [S5]$$

and

$$\theta_3 + \theta_4 = \cos^{-1}(\cos\theta_3' \cos\phi) + \cos^{-1}(\cos\theta_4' \cos\phi). \qquad [S6]$$

Now observe that $\theta_3 + \theta_4$ monotonically approaches π as ϕ goes from zero to $\pi/2$. The sign of $d/d\phi(\theta_3 + \theta_4)$ is determined by which projected angle θ_3' or θ_4' deviates most from $\pi/2$ (i.e. if $|\pi/2 - \theta_3'| > |\pi/2 - \theta_4'|$ then $\text{sgn}[d/d\phi(\theta_3 + \theta_4)] = \text{sgn}[\pi/2 - \theta_3']$). This follows from the negative monotonicity and symmetry of inverse cosine about $\pi/2$. So $\theta_3 + \theta_4$ begins at an endpoint of the interval $[\beta, 2\pi - \beta]$ when $\phi = 0$ and approaches π monotonically within the same interval as $\phi \to 0$. This parameterizes all angle pairs in space and thus $\beta \leq \theta_3 + \theta_4 \leq 2\pi - \beta$.

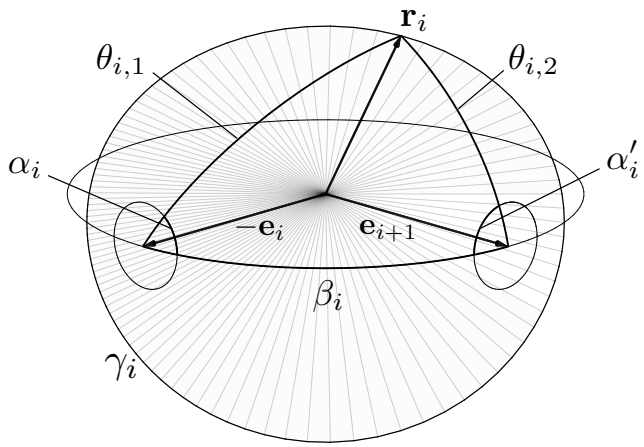

Fig. S4. Location of α is arbitrary. Each value of α_i uniquely determines a point on the γ curve, which in turns uniquely determines a value of α_i', the angle from the β plane and the $\theta_{i,2}$ plane, left-hand oriented about the growth front edge $\mathbf{e}_{i+1}$. α_i' shares an axis with α_{i+1}, so a given α_i uniquely determines α_{i+1}.

A.3. Angle sum solutions are unique. For uniqueness, we need to show that f is positive monotonic on the interval $\theta_1 \in [\beta, 2\pi - \beta]$. This amounts to showing that $|d\theta_2(\theta_1)/d\theta_1| \leq 1$ or, equivalently, $(d\theta_2(\theta_1)/d\theta_1)^2 \leq 1$. Recalling that $\theta_2(\theta_1) = \cos^{-1}(\cos\theta_1 \cos\beta + \sin\theta_1 \sin\beta \cos\alpha)$, we have

$$\frac{d\theta_2}{d\theta_1} = \frac{\sin\theta_1 \cos\beta - \cos\theta_1 \sin\beta \cos\alpha}{\sqrt{1 - (\cos\theta_1 \cos\beta + \sin\theta_1 \sin\beta \cos\alpha)^2}} \quad [S7]$$

and hence

$$\left(\frac{d\theta_2}{d\theta_1}\right)^2 = \frac{(\sin\theta_1 \cos\beta - \cos\theta_1 \sin\beta \cos\alpha)^2}{1 - (\cos\theta_1 \cos\beta + \sin\theta_1 \sin\beta \cos\alpha)^2} = \frac{\cos^2\beta + \sin^2\beta \cos^2\alpha - K^2}{1 - K^2} \leq 1, \quad [S8]$$

where $K = \cos\theta_1 \cos\beta + \sin\theta_1 \sin\beta \cos\alpha$ and equality occurs only for $\alpha = 0, \pi$. Thus $f(\theta_1)$ is positive monotonic on $\theta_1 \in [\beta, 2\pi - \beta]$ and solutions $f(\theta_1) = k$ are unique for all values $\beta \neq 0, \pi$.

A.4. Any flap angle location explores the full design space. One detail in this construction remains, which is the question of whether choosing different locations for the flap angle will yield different spaces of possible new designs. If this were true, it would complicate the search at each additive design step, requiring the designer / algorithm to explore design spaces yielded by varying the flap angle at each new quad and to collate the results before choosing a new design. Fortunately, this is not the case: all choices of quad locations for the flap angle are equivalent, so exploring α values at any location along the growth front explores the full space of possible designs at that front. Let α_i be the flap angle at the chosen location along strip (dihedral angle between $\theta_{i,1}$ face and β_i face, left-hand oriented about the growth front edge $\mathbf{e}_i$), α_i' be the angle from the β plane and the $\theta_{i,2}$ plane, left-hand oriented about the growth front edge $\mathbf{e}_{i+1}$ (see Fig. S4). Solutions of the angle sum constraint $\theta_{i,1} + \theta_{i,2} = k_i$ form an ellipse of spherical arcs γ_i. The foci of this ellipse are given by the edges that define the β face, i.e. the boundary edges $\mathbf{e}_i$ and $\mathbf{e}_{i+1}$ of the growth front and the axes of α_i and α_i', respectively. Clearly, any choice of $\alpha_i \in [0, 2\pi)$ yields a unique $\alpha_i' \in [0, 2\pi)$, which is related to the next flap angle α_{i+1} by a constant phase shift given by the dihedral angle between the β_i and β_{i+1} planes. Thus sweeping α_i through the interval $[0, 2\pi)$ also sweeps α_{i+1} uniquely through the same interval. This establishes a bijective mapping between two consecutive flap angles, which in turn determine new interior angles along the entire growth front. So the choice of which quad along the strip to pick as the flap angle location is arbitrary: any sweeping the flap angle at any quad location along the strip will explore the full space of possible new interior strip geometries uniquely.

B. Adaptations of strip construction. While it is trivial to growth a simple patch of quad origami by adding strips in any order to its four boundaries, the strip construction can be adapted, in most cases by sacrificing some degrees of freedom, to alternative surface geometries and topologies. We illustrate two cases here, non-convex patches and closed loops, and leave further adaptations for future work. Notably, the degree of freedom associated with flap angle choice becomes determined in both of these examples.

B.1. Concave corner. For a surface patch with a concave corner formed by a row of boundary points $\mathbf{x}_i, i \in \{0, n\}$ and a column of boundary points $\mathbf{y}_j, j \in \{0, \ldots, m\}$ such that $\mathbf{x}_0 = \mathbf{y}_0$ is the corner, we adapt the strip algorithm to add a pair of strips originating at this corner by determining growth directions $\mathbf{r}_i$ and $\mathbf{t}_j$ for the x and y boundaries, respectively (see Fig. S5). It is clear that the plane containing $\mathbf{x}_0$, $\mathbf{x}_1$, $\mathbf{y}_0$ and $\mathbf{y}_1$ determines the flap angle needed to calculate both $\mathbf{r}_1$ and $\mathbf{t}_1$. So all interior growth directions $\mathbf{r}_i, i \in \{i, \ldots, n-1\}$ and $\mathbf{t}_j, j \in \{j, \ldots, m-1\}$ are determined by the existing surface geometry. The boundary growth directions $\mathbf{r}_n$ and $\mathbf{t}_m$ can be chosen freely in the plane of $\mathbf{x}_{n-1}$, $\mathbf{x}_n$ and $\mathbf{r}_{n-1}$ and the plane of $\mathbf{y}_{m-1}$, $\mathbf{y}_m$ and $\mathbf{t}_{m-1}$, respectively. Finally, the edge lengths at $\mathbf{x}_i, i \in \{2, \ldots, n\}$ and $\mathbf{y}_j, j \in \{2, \ldots, m\}$ may be chosen freely within the usual

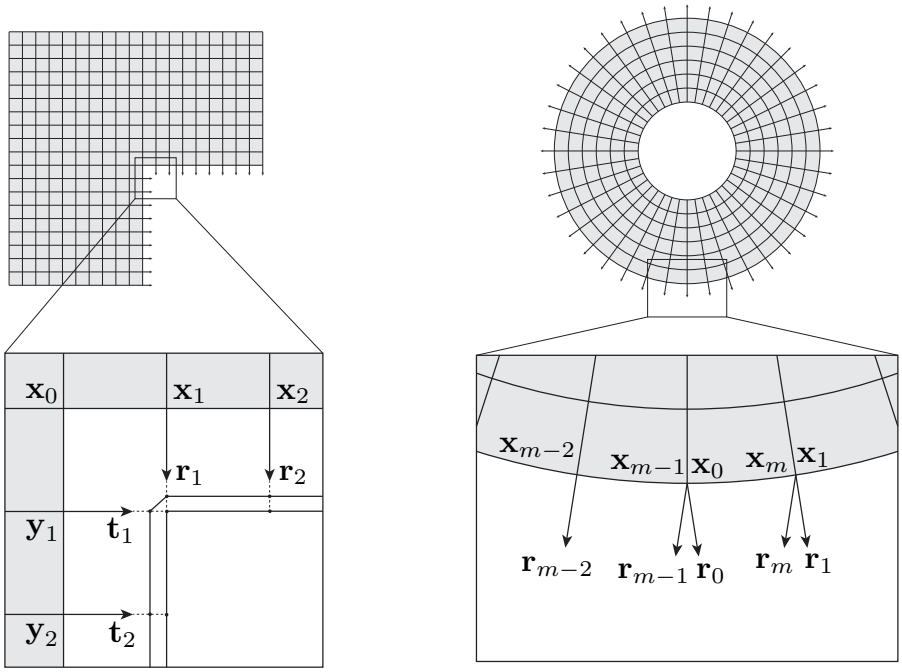

Fig. S5. Adaptations of strip construction. (Left) For a concave corner formed by a row of boundary points $\mathbf{x}_i, i \in \{0, n\}$ and a column of boundary points $\mathbf{y}_j, j \in \{0, \dots, m\}$ with $\mathbf{x}_0 = \mathbf{y}_0$, the lengths of the new edges at $\mathbf{x}_1$ and $\mathbf{y}_1$ are bounded additionally by the possible intersection of the growth directions $\mathbf{r}_1$ and $\mathbf{t}_1$. One can choose the edge lengths at these locations to match their intersection lengths, or add a new edge to the growth front at the corner to make it five-coordinated. **(Right)** For a closed loop consisting of $m-1$ quads, we treat the growth front as consisting of $m+1$ vertices $\mathbf{x}_i, i \in \{0, \dots, m\}$ with two overlapping pairs $(\mathbf{x}_0, \mathbf{x}_{m-1})$ and $(\mathbf{x}_1, \mathbf{x}_m)$, such that the boundary growth directions $\mathbf{r}_0$ and $\mathbf{r}_m$ overlap with the interior growth directions $\mathbf{r}_{m-1}$ and $\mathbf{r}_1$ respectively. We then search for flap angles which give $\mathbf{n}_1 = \mathbf{n}_m$, where $\mathbf{n}_i$ is the unit normal of the i^{th} new quad.

local intersection bounds. The lengths of new edges at $\mathbf{x}_1$ and $\mathbf{y}_1$ are bounded additionally by the possible intersection of $\mathbf{r}_1$ and $\mathbf{t}_1$. If edge lengths at these locations are not chosen to match their intersection lengths, then a new edge will be added to the growth front at the corner, the corner face will be five-coordinated rather than four (a defect) and the next growth front will be simple rather a corner.

B.2. Closed loop. For a surface patch having a growth front formed by a single closed loop of quads, we adapt the strip algorithm to attach a new closed loop of quads at this boundary by searching for closure conditions around the loop. Let the growth front consist of $m-1$ quads, then we can treat the growth front as consisting of $m+1$ vertices $\mathbf{x}_i, i \in \{0, \dots, m\}$ where the pairs $(\mathbf{x}_0, \mathbf{x}_{m-1})$ and $(\mathbf{x}_1, \mathbf{x}_m)$ each describe the same vertex, i.e. these labels overlap (see Fig. S5). This gives a simple growth front with boundary growth directions $\mathbf{r}_0$ and $\mathbf{r}_m$ overlapping with interior growth directions $\mathbf{r}_{m-1}$ and $\mathbf{r}_1$, respectively. This setup allows us to search for flap angles which give $\mathbf{n}_1 = \mathbf{n}_m$, where $\mathbf{n}_i$ is the unit normal of the i^{th} new quad. The continuation solution is guaranteed to exist, and other solutions to this closure condition give non-trivial folds at the growth front.

S2. Special vertices

A. Angle conditions. We derive the flap angle values that produce flat-foldable, equal new design angles, continuation/reflection and locked single vertices. First, we derive the closed-form single vertex solution from the main text using the law of cosines for the spherical triangle formed by $\theta_{i,1}$, $\theta_{i,2}$ and β_i and a cosine identity.

$$\cos\theta_{i,2} = \cos\left(k_i - \theta_{i,1}\right) \tag{S9}$$

$$\cos\theta_{i,1}\cos\beta_i + \sin\theta_{i,1}\sin\beta_i\cos\alpha_i = \cos k_i\cos\theta_{i,1} + \sin k_i\sin\theta_{i,1} \tag{S10}$$

$$\cos\beta_i + \tan\theta_{i,1}\sin\beta_i\cos\alpha_i = \cos k_i + \sin k_i\tan\theta_{i,1} \tag{S11}$$

$$\tan\theta_{i,1}(\sin\beta_i\cos\alpha_i - \sin k_i) = \cos k_i - \cos\beta_i \tag{S12}$$

$$\tan\theta_{i,1} = \frac{\cos k_i - \cos\beta_i}{\sin\beta_i\cos\alpha_i - \sin k_i}. \tag{S13}$$

We now have a relationship between one of the new design angles and the flap angle, so special vertex solutions given only by design angles conditions follow, so long as $(k_i - \beta_i)/2 \leq \theta_{i,1} \leq (k_i + \beta_i)/2$.

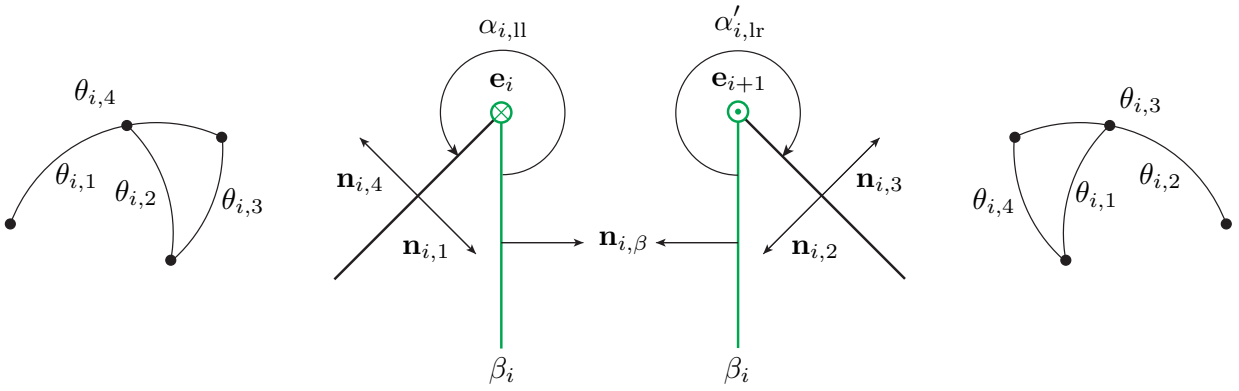

Fig. S6. Locked configurations. (Left) A locked left vertex has coplanar faces containing θ_1 and θ_4. The flap angle $\alpha_{i,\mathrm{ll}}$ rotates $\mathbf{n}_{i,\beta}$ to $\mathbf{n}_{i,1} = -\mathbf{n}_{i,4}$ about $\mathbf{e}_i$, shown oriented into the page. **(Right)** A locked right vertex has coplanar faces containing $\theta_{i,2}$ and $\theta_{i,3}$. The angle $\alpha'_{i,\mathrm{lr}}$ rotates $\mathbf{n}_{i,\beta}$ to $\mathbf{n}_{i,2} = -\mathbf{n}_{i,3}$ about $\mathbf{e}_{i+1}$, shown oriented out of the page.

flat-foldable (Kawasaki (2))	$\theta_1 + \theta_3 = \theta_2 + \theta_4 = \pi$	$\cos\alpha_{ff} = \frac{1}{\sin\beta}\left(\sin k + \frac{\cos\beta - \cos k}{\tan\theta_3}\right)$
equal design angles	$\theta_1 = \theta_2 = k/2$	$\cos\alpha_{eq} = \frac{1}{\sin\beta}\left(\sin k - \frac{\cos\beta - \cos k}{\tan(k/2)}\right)$
continuation	$\theta_1 + \theta_4 = \theta_2 + \theta_3 = \pi$	$\cos\alpha_{con} = \frac{1}{\sin\beta}\left(\sin k + \frac{\cos\beta - \cos k}{\tan\theta_4}\right)$

B. Locked configurations. A single vertex origami is trivially locked when $\alpha_i \in \{0, \pi\}$, i.e. the β_i, $\theta_{i,1}$ and $\theta_{i,2}$ faces are coplanar. Non-trivial locked configurations occur when one of the new faces in the vertex is coplanar with an existing face. These special vertices depend on the orientation of the existing faces in three-dimensional space, so their flap angles cannot be derived from the above design/flap angle relation. The left locked configuration occurs when face normals $\mathbf{n}_{i,1}$ and $\mathbf{n}_{i,4}$ belonging to $\theta_{i,1}$ and $\theta_{i,4}$ faces, respectively, satisfy $\mathbf{n}_{i,1} = -\mathbf{n}_{i,4}$ (see Fig. S6). We write down the flap angle $\alpha_{i,\mathrm{ll}}$ that gives a such a vertex by inspecting the arrangement of $\mathbf{n}_{i,1}$, $\mathbf{n}_{i,4}$ and $\mathbf{n}_{i,\beta}$ about their common axis, the growth front edge $\mathbf{e}_i$ between the faces containing $\theta_{i,1}$ and $\theta_{i,4}$:

$$\alpha_{i,\mathrm{ll}} = \mathrm{mod}\Big(\mathrm{atan2}\big((\mathbf{n}_{i,\beta} \times \mathbf{n}_{i,4}) \cdot \mathbf{e_i}, -\mathbf{n}_{i,\beta} \cdot \mathbf{n}_{i,4}\big), 2\pi\Big). \quad [S14]$$

The right locked configuration occurs when face normals n_2 and n_3 belonging to θ_2 and θ_3 faces, respectively, satisfy $\mathbf{n}_{i,2} = -\mathbf{n}_{i,3}$. We write down the angle $\alpha'_{i,\mathrm{lr}}$ by inspecting the arrangement of $\mathbf{n}_{i,2}$, $\mathbf{n}_{i,3}$ and $\mathbf{n}_{i,\beta}$ about their common axis, the growth front edge $\mathbf{e}_{i+1}$ between the faces containing $\theta_{i,2}$ and $\theta_{i,3}$:

$$\alpha'_{i,\mathrm{lr}} = \mathrm{mod}\Big(\mathrm{atan2}\big((\mathbf{n}_{i,\beta} \times \mathbf{n}_{i,3}) \cdot \mathbf{e}_{i+1}, -\mathbf{n}_{i,\beta} \cdot \mathbf{n}_{i,3}\big), 2\pi\Big). \quad [S15]$$

The flap angle $\alpha_{i,\mathrm{lr}}$ that gives a locked right vertex can then be calculated from $\alpha'_{i,\mathrm{lr}}$. Calculating $\theta_{i,2}$ from $\tan\theta_{i,2} = (\cos\beta_i - \cos k_i)/(\sin k_i - \sin\beta_i \cos\alpha'_i)$ and using the spherical laws of cosines and sines for the spherical triangle formed by $\theta_{i,1}$, $\theta_{i,2}$ and β_i, we have

$$\alpha_{i,\mathrm{lr}} = \mathrm{mod}\Big(\mathrm{atan2}\big(\frac{\sin\theta_{i,2}}{\sin\theta_{i,1}}\sin\alpha'_{i,\mathrm{lr}}, \frac{\cos\theta_{i,2} - \cos\theta_{i,1}\cos\beta_i}{\sin\theta_{i,1}\sin\beta_i}\big), 2\pi\Big). \quad [S16]$$

We also observe that a single vertex origami is self-intersecting when $(\mathbf{r} \cdot \hat{n}_3)(\mathbf{r} \cdot \hat{n}_4) < 0$ and $\mathbf{r} \cdot \bar{\mathbf{r}} < 0$, which occurs when $\alpha \in (\pi, \min(\alpha_{ll}, \alpha_{lr})) \bigcup (\max(\alpha_{ll}, \alpha_{lr}), 2\pi)$ if $\hat{n}_\beta \cdot \bar{\mathbf{r}} > 0$ or $\alpha \in (0, \min(\alpha_{ll}, \alpha_{lr})) \bigcup (\max(\alpha_{ll}, \alpha_{lr}), \pi)$ if $\hat{n}_\beta \cdot \bar{\mathbf{r}} < 0$.

S3. Edge length bounds

For each new quad along the growth front incident to new design angles $\theta_{i,2}$ and $\theta_{1,i+1}$ and new edge directions $\mathbf{r}_i$ and $\mathbf{r}_{i+1}$, if

$$\theta_{i,2} + \theta_{1,i+1} < \pi, \quad [S17]$$

the lines $\mathbf{p}_i(t_i) = \mathbf{x}_i + t_i\mathbf{r}_i$ and $\mathbf{p}_{i+1}(s_i) = \mathbf{x}_{i+1} + s_i\mathbf{r}_{i+1}$ will intersect for some positive t_i and s_i (see Fig. S7). Their intersection gives a bound on the edge length choices l_i and l_{i+1}, which we can locate by minimizing the distance D between $\mathbf{p}_i$ and $\mathbf{p}_{i+1}$ with respect to t and s:

$$D(t_i, s_i) = ||\mathbf{p}_i(t_i) - \mathbf{p}_{i+1}(s_i)||_2. \quad [S18]$$

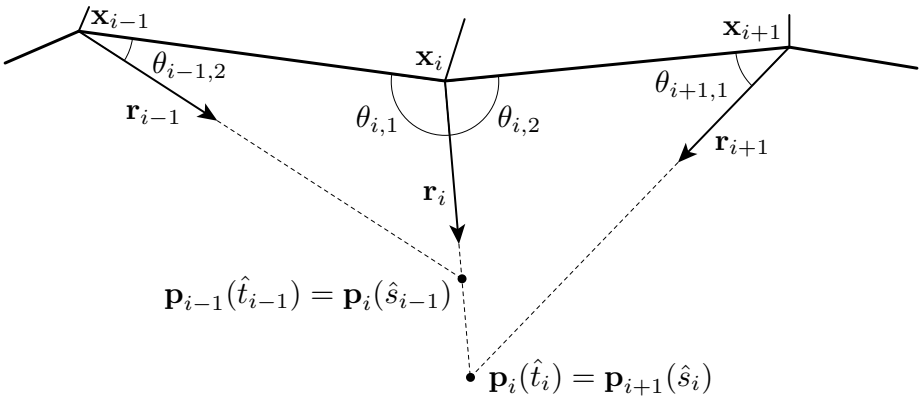

Fig. S7. Edge length bounds. Two new quads (gray) along a growth front will be formed by selecting lengths l_{i-1}, l_i and l_{i+1} for edges parallel to the solved directions $\mathbf{r}_{i-1}$, $\mathbf{r}_i$ and $\mathbf{r}_{i+1}$, respectively. Eq. (S17) is satisfied for both quads, so bounds are calculated by determining the intersections $\mathbf{x}$ of the new edge directions.

Note that this formulation is valid for skew rays in $\mathbb{R}^3$, but because $\mathbf{r}_i$ and $\mathbf{r}_{i+1}$ are coplanar by construction we expect to find positive t and s such that $D(t,s) = 0$ if Eq. (S17) holds. For simplicity, we can minimize D^2 directly:

$$\nabla D^2(t_i, s_i) = 0, \tag{S19}$$

producing a system of two linear equations in t and s, which can be inverted analytically:

$$\begin{bmatrix} \hat{t}_i \\ \hat{s}_i \end{bmatrix} = \frac{1}{1-(\mathbf{r}_i \cdot \mathbf{r}_{i+1})^2} \begin{bmatrix} 1 & \mathbf{r}_i \cdot \mathbf{r}_{i+1} \\ \mathbf{r}_i \cdot \mathbf{r}_{i+1} & 1 \end{bmatrix} \begin{bmatrix} (\mathbf{x}_{i+1} - \mathbf{x}_i) \cdot \mathbf{r}_i \\ (\mathbf{x}_i - \mathbf{x}_{i+1}) \cdot \mathbf{r}_{i+1} \end{bmatrix}. \tag{S20}$$

Plugging the solved values $\hat{t}_i$ and $\hat{s}_i$ back into p_i and p_{i+1} gives the point of intersection of the new ray directions in $\mathbb{R}^3$, so t_i and s_i bound l_i and l_{i+1}, respectively. Now, each new interior edge direction $\mathbf{r}_i$ (where $i \neq 0$ and $i \neq m$) is incident to two new quads and could intersect either new edge direction $\mathbf{r}_{i-1}$ or $\mathbf{r}_{i+1}$. So we must apply t and s bounds from the preceding (t_{i-1}, s_{i-1}) and following (t_i, s_i) quads in the strip to give our final bound on l_i:

$$l_i \leq \min(s_{i-1}, t_i). \tag{S21}$$

S4. Applications

We implement our strip construction in inverse design frameworks to design a variety of quad origami surfaces (see Figs. S8 and S9 for high-resolution images of the mountain-valley assignments for the patterns from Fig. 4 of the main text). The applications differ only in their input seeds and how the DOFs identified by the strip construction are chosen. Our design frameworks tend to focus on the flap angle, and thereby the growth direction of the front, as the key DOF. Boundary design angles and edge lengths, the other DOFs of the strip construction, are typically chosen after a flap angle is determined and in that order. Although this ordering is not strictly necessary, it follows naturally from the observation that the new transverse edge lengths in the strip are bounded by local self-intersection of the growth directions. Of course, alternative DOF selection patterns are possible, for example the selection of edge lengths before all growth directions are determined, but such an implementation will inevitably be more complicated as local self-intersection bounds must then be observed retroactively and the predetermined edge lengths may therefore need to be modified. We begin our discussion with a detailed look at edge length bounds from local self-intersection of growth directions and then describe in detail three surface design applications: surface fitting by inverse design of generalized Miura-ori tessellations, inverse design of curved fold models and disordered or "crumpled" sheets.

A. Surface fitting (main text Fig. 4A). Returning to the inverse problem of origami surface approximations, we harness this novel additive construction to fit generalized Miura-ori tessellations to curved surfaces. Given a smooth target surface, we consider two surfaces displaced in the normal direction from the target surface (upper and lower), forming a sandwich structure. A simple singly-corrugated strip is constructed as a seed, with one side lying on the upper surface and one side on the lower surface. We then add strips to either side of the seed additively such that all nodes on the upper side of the origami surface fall exactly on the upper corrugating surface and all nodes on the lower side of the origami patch fall exactly on the lower corrugating surface. This novel approach is perfectly tailored to design origami sandwich structures that reside in the interstice of the two smooth surfaces (see Fig. S10). Consider a target surface $\mathbf{X}(u,v)$ with surface normal vector $\mathbf{n}(u,v)$. A normal surface $\mathbf{X}_h(u,v)$ is given by displacing the target surface in the direction of its normal field by a constant thickness h: $\mathbf{X}(u,v) + h\mathbf{n}(u,v)$. We construct upper $\mathbf{X}_{\epsilon/2}$ and lower $\mathbf{X}_{-\epsilon/2}$ normal surfaces each displaced by a distance of $\epsilon/2$ from the target surface to give a

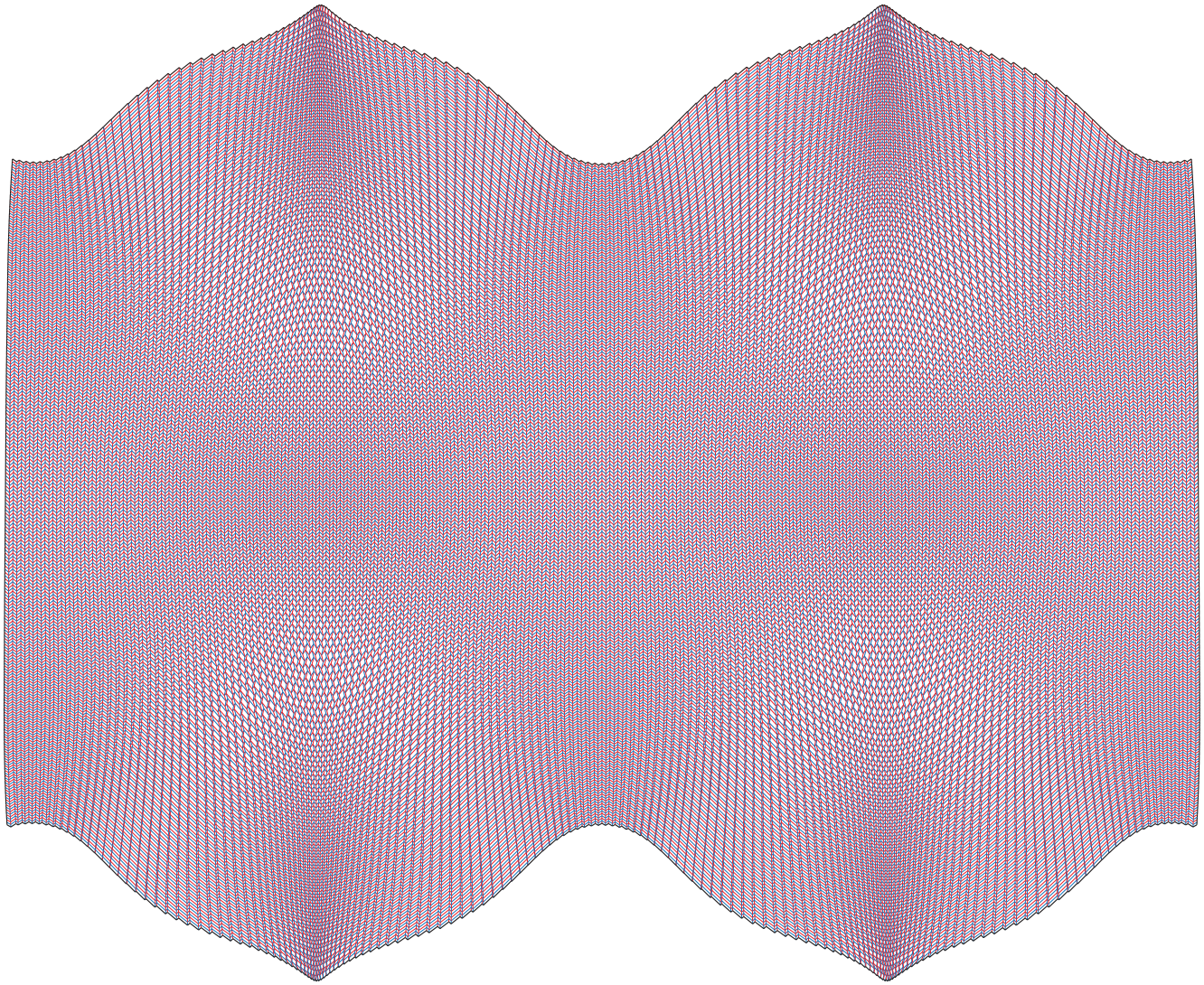

Fig. S8. The mountain-valley pattern of the model in Fig. 4A in the main text.

volume with constant thickness ϵ. Note that ϵ is a tunable parameter that controls how close the origami structure is to the target surface. The surface example in Fig. 4A in the main text is given by

$$\mathbf{X}(u,v) =< u, v, H\sin(Au)\cos(Av) >, \tag{S22}$$

with shape parameters $H = 0.2$ and $A = 1.05\pi$, thickness $\epsilon = 2/m$ and seed resolution $m = 40$.

We initialize two rows of coordinates $< u_{i,0}, v_{i,0} >$ and $< u_{i,1}, v_{i,1} >$ according to

$$< u_{i,j}, v_{i,j} > =< (-1)^i \frac{c}{2} + (-1)^j \frac{1}{m}, -1 + \frac{i}{m} >, \tag{S23}$$

with $i \in \{0, \ldots, m\}$ and $j \in \{0, 1\}$. Evaluating $\mathbf{X}_{-\epsilon/2}(u_{i,0}, v_{i,0})$ and $\mathbf{X}_{\epsilon/2}(u_{i,1}, v_{i,1})$ gives two rows of points in space, one on each of the upper and lower surfaces, which define a strip of quads whose faces are nearly, but not exactly, planar. To polish the geometry of the strip before it becomes a growth seed, we collect the set of rays $\mathbf{r}_i$ and lengths l_i:

$$\mathbf{a}_i = \mathbf{X}_{\epsilon/2}(u_{i,1}, v_{i,1}) - \mathbf{X}_{-\epsilon/2}(u_{i,0}, v_{i,0}), \tag{S24}$$

$$l_i = \|\mathbf{a}_i\|_2, \tag{S25}$$

and use Matlab's `fmincon` to minimize the objective function

$$C(\mathbf{b}) = \sum_{i=0}^{m} 1 - \frac{\mathbf{a}_i \cdot \mathbf{b}_i}{l_i} \tag{S26}$$

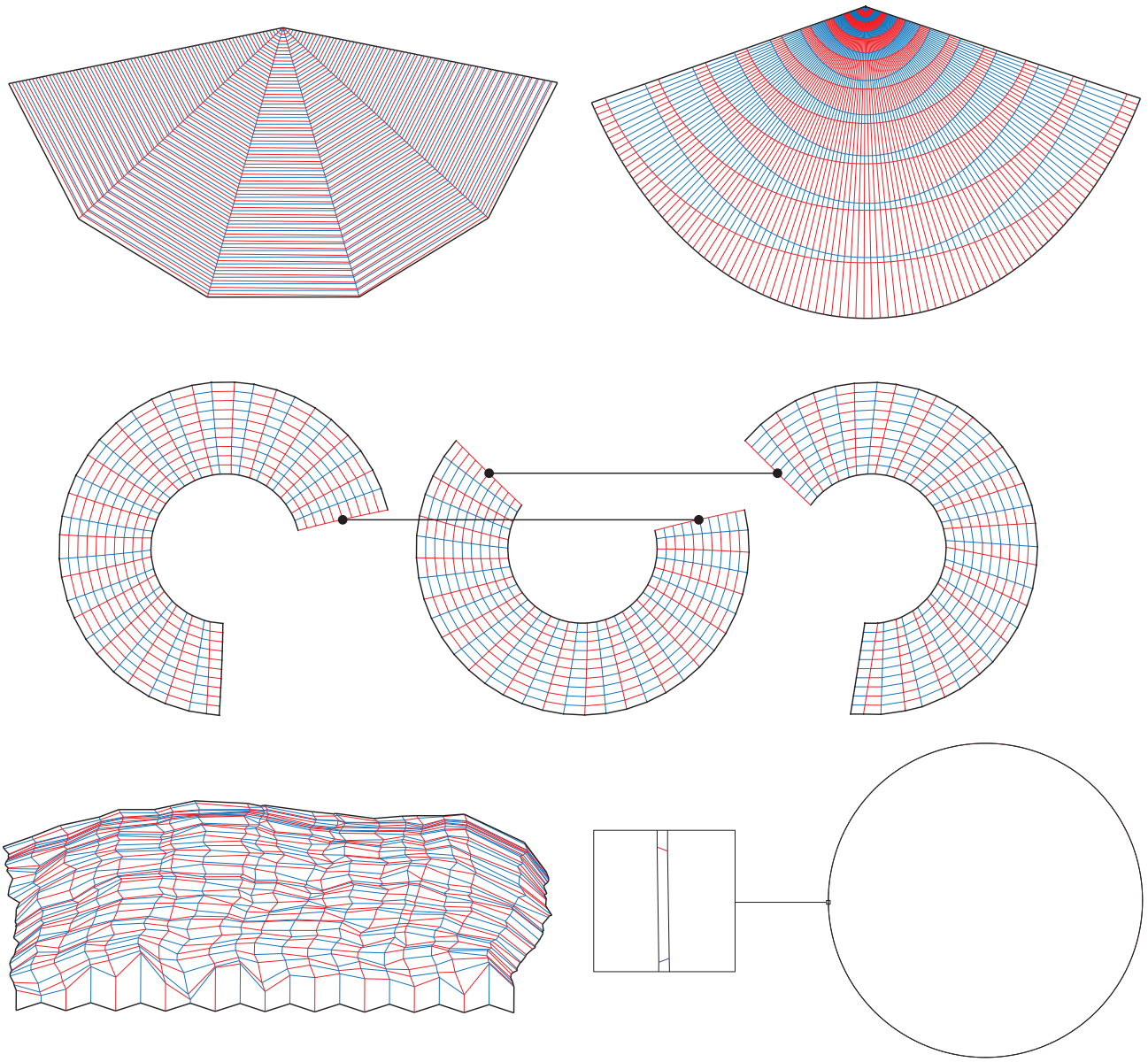

Fig. S9. The mountain-valley patterns of the models in Figs. 4B–F in the main text. (Top left) Fig. 4B. **(Top right)** Fig. 4C. **(Middle)** Fig. 4D. **(Bottom left)** Fig. 4E. **(Bottom right)** Fig. 4F.

subject to the constraints

$$\|\mathbf{b}_i\|_2 - 1 = 0, i \in \{0, \dots, m\}, \tag{S27}$$

$$(\mathbf{b}_i \times \mathbf{b}_{i+1}) \cdot \mathbf{e}_i = 0, i \in \{0, \dots, m-1\}, \tag{S28}$$

where

$$\mathbf{e}_i = \frac{\mathbf{X}_{-\epsilon/2}(u_{i+1,0}, v_{i+1,0}) - \mathbf{X}_{-\epsilon/2}(u_{i,0}, v_{i,0})}{\|(\mathbf{X}_{-\epsilon/2}(u_{i+1,0}, v_{i+1,0}) - \mathbf{X}_{-\epsilon/2}(u_{i,0}, v_{i,0}))\|_2}. \tag{S29}$$

This allows us to construct our final Miura-type seed from the modified strip of quads with exactly planar faces whose two boundary rows are the original $\mathbf{X}_{-\epsilon/2}(u_{i,0}, v_{i,0})$ and the polished $\mathbf{X}_{-\epsilon/2}(u_{i,0}, v_{i,0}) + l_i \mathbf{b}_i$. In practice, this results in the polished row of points being offset slightly from the bounding surface, so we adjust l_i according to the line/surface intersection routine described in Section S4A.2 below such that all points in the seed fall on the upper or lower surfaces.

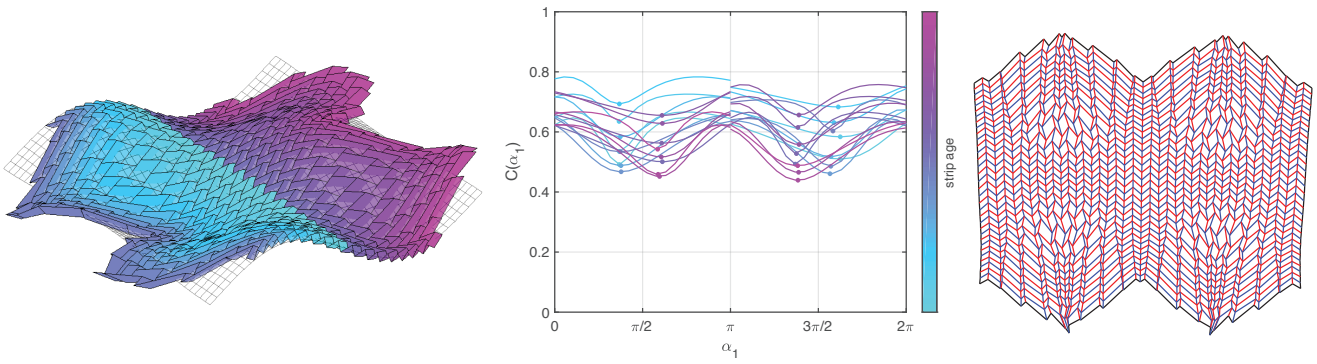

Fig. S10. Surface fitting construction. (Left) The seed strip (outlined in black) and the target surface. **(Middle)** Flap angles optimization. **(Right)** The mountain-valley folding pattern.

A.1. Choosing the angles. Now we proceed to grow the singly-corrugated seed by using the strip construction to determine compatible strips at its two boundaries, one of which lies on each of the lower and upper surfaces. In general, we seek a flap angle that gives growth directions toward the lower surface for the upper growth front and toward the upper surface for the lower growth front. That is, we seek to induce a second, transverse corrugation in the origami surface by reflecting, at least in a qualitative sense, its growth back and forth in the interstice of the upper and lower target surfaces. To accomplish this, we write down bounds on the flap angle that constrain the growth of the surface to this interstice, and optimize the resultant design angles within these bounds and with respect to the flap angle. A cost function that avoids extreme design angles is given by

$$C(\alpha_1) = \sum_{i=1}^{m-1} \big(\theta_{i,1}(\alpha_1) - \pi/2\big)^2 + \big(\theta_{i,2}(\alpha_1) - \pi/2\big)^2, \qquad [S30]$$

and α_i is bounded to the interval $(0, \pi)$ or $(\pi, 2\pi)$ depending on the orientation of the flap angle location relative to the upper or lower surface. In practice, we perform a linear grid search of $C(\alpha_1)$ over the valid interval to visualize the behavior of the cost function, then polish the optimal evaluated flap angle by passing it as an initial value along with the above cost function and bounds to Matlab's `fmincon`.

Boundary design angles are chosen such that the boundary growth directions $\mathbf{r}_0$ and $\mathbf{r}_m$ are parallel to their adjacent interior rays $\mathbf{r}_1$ and $\mathbf{r}_{m-1}$, respectively.

A.2. Choosing the edge lengths. Edge lengths are chosen such that the next row of points lies exactly on the other corrugating surface, either lower or upper, via a numerical projection routine that computes intersections between rays and a surface. Consider a surface $\mathbf{X}(u, v)$ with unit normal $\mathbf{n}(u, v)$ and a line $\mathbf{L}(t) = \mathbf{p} + t\mathbf{v}$. For a given t, we can calculate the distance from a point on the line to the surface by finding $\hat{u}(t), \hat{v}(t)$ that minimizes $d(u, v) = \|\mathbf{X}(u, v) - \mathbf{L}(t)\|_2$. We find the intersection of the line and the surface, if it exists and is well-defined, by minimizing

$$d(t) = \|\mathbf{X}(\hat{u}(t), \hat{v}(t)) - \mathbf{L}(t)\|_2 \qquad [S31]$$

using Matlab's constrained optimization routine `fmincon` in order to bound $t \geq 0$ during minimization.

We note that in the formulation above, the target surface is parameterized using two parameters u, v. We remark that any other representation of the surface (in the form of an explicit function, an implicit function, a triangular mesh, a quad mesh etc.) can also be used as long as the surface normal (for constructing the upper and lower surfaces) and the point-to-surface distance (for optimizing the edge lengths) can be computed from it.

A gallery of origami surface fitting results created by our additive approach are presented in Fig. S11. It can be observed that our additive approach is capable of approximating surfaces with different curvature properties. Moreover, our approach allows for the creation of very high resolution models, which are nearly impossible to discover using a global optimization scheme due to the computational complexity. We note that increasing the resolution of the approximating origami surface naturally decreases the amount of integrated Gauss curvature each cell in the origami surface needs to accommodate. This suggests that as resolution increases and the characteristic length of the approximating Miura-ori cell becomes vanishingly small compared to the radii of principle curvatures of the target surface, the surface starts to look like its tangent plane and the surface fitting problem becomes trivial, locally.

One may ask whether every target surface admits a unique origami approximant under our framework. As shown in Fig. S11, one can change the resolution of the seed strip to achieve different fold patterns for the same target surface. Fig. S12 shows two origami structures with the same resolution (same number of vertices and same number of quads) approximating the

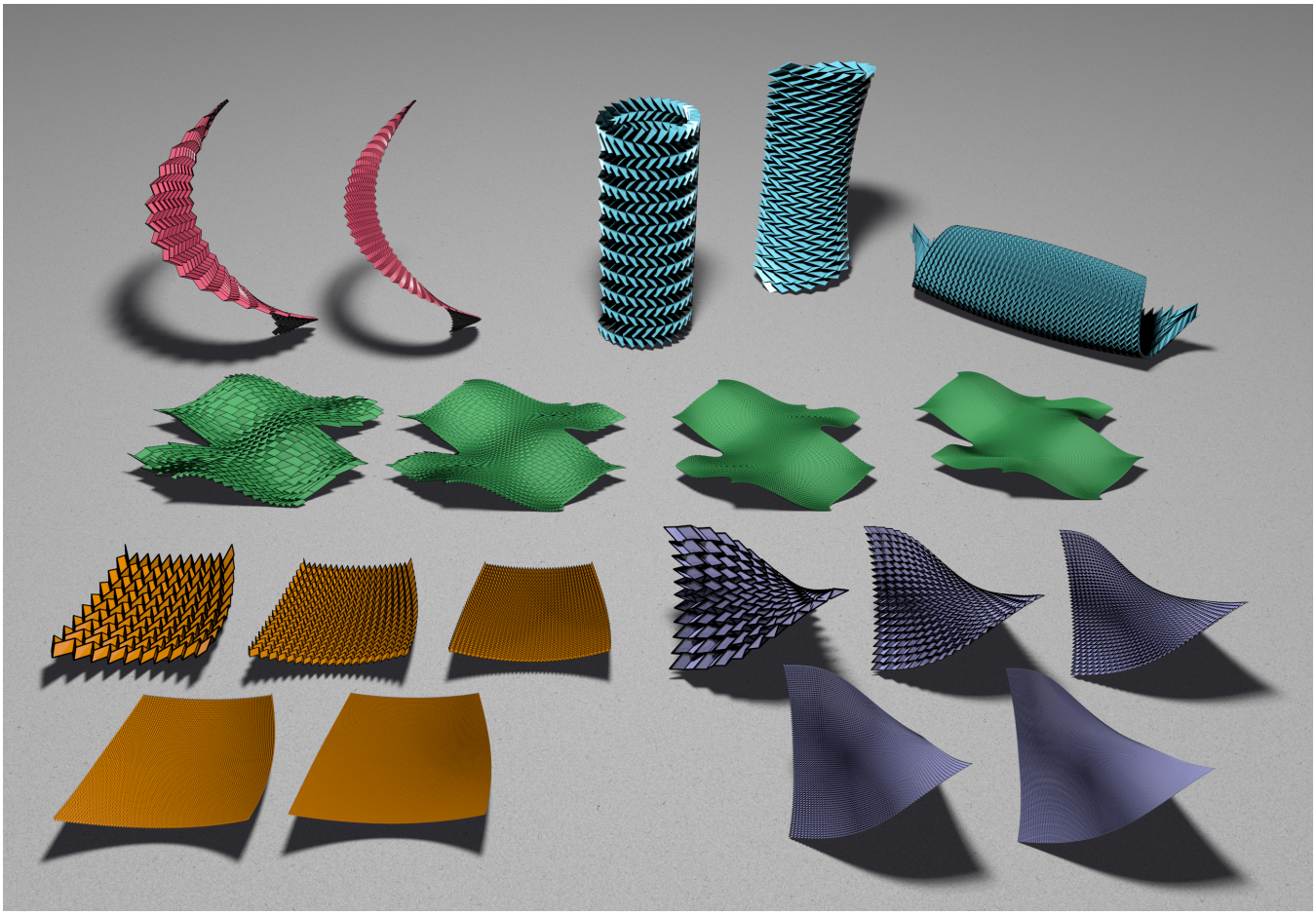

Fig. S11. Additional surface fitting results. We deploy our additive approach to approximate a large variety of surfaces, including a helicoid at two different resolutions (top left), cylinders with different Gaussian curvatures (zero/negative/positive as shown in top right), a landscape shape with mixed curvature at four different resolutions (the middle row), a paraboloid at five different resolutions (bottom left), and a hypar at five different resolutions (bottom right).

same target surface obtained by our additive framework. The seed strips of the two structures are set to be with different corrugation widths, and it can be observed that both the 3D folded structures and the 2D crease patterns are significantly different. This shows that our additive framework is capable of producing multiple surface-fitting origami structures even with the same resolution.

B. Twisted plane models (main text Figs. 4B,C). We describe here details from the nested cone example presented in Fig. 4C in the main text and display several other examples as well. Consider an upside-down cone of height h with origin $\mathbf{p} =< 0, 0, -h/2 >$ and base described by the circle $\mathbf{f}(t) =< A\cos t, A\sin t, h/2 >$ where $A = h\tan(\theta/2)$. Following the closed loop growth pattern described in Section S1B.2, we construct a strip of m quads with overlapping end faces by sampling

$$\mathbf{x}_i = \mathbf{f}\Big(2i\pi\big(1+\frac{1}{m-2}\big)\Big), i \in \{0,\dots,m-1\}, \quad [S32]$$

$$\mathbf{y_i} = 0.01\mathbf{x}_i + 0.99p, \quad [S33]$$

where $\mathbf{x}_i$ forms the growth front and $\mathbf{y}_i$ is the truncated point of the cone. The Huffman nested cones model in the main text (Fig. 4C) uses $m = 102$, $h = 1$ and $\theta = \pi/4$. The twisted squares model in the main text (Fig. 4B) uses $m = 6$, $h = .1$ and $\theta = \pi/4$.

We use a simple design angle difference cost function to search for flap angles α_1 that regularize the pattern design:

$$C(\alpha_1) = \frac{1}{2(m-1)\pi^2}\sum_{i=1}^{m-2}\sum_{j=1}^{2}(\theta_{i,j} - \theta_{i+1,j})^2. \quad [S34]$$

In both cases, we use neighborhoods of minima of a continuation avoidance cost function (shown as dashed curves in Fig. S13)

$$C_{\text{con}}(\alpha_1) = \frac{1}{m-1}\sum_{i=1}^{m-1}\bar{\mathbf{r}}_i \cdot \mathbf{r}_i, \quad [S35]$$

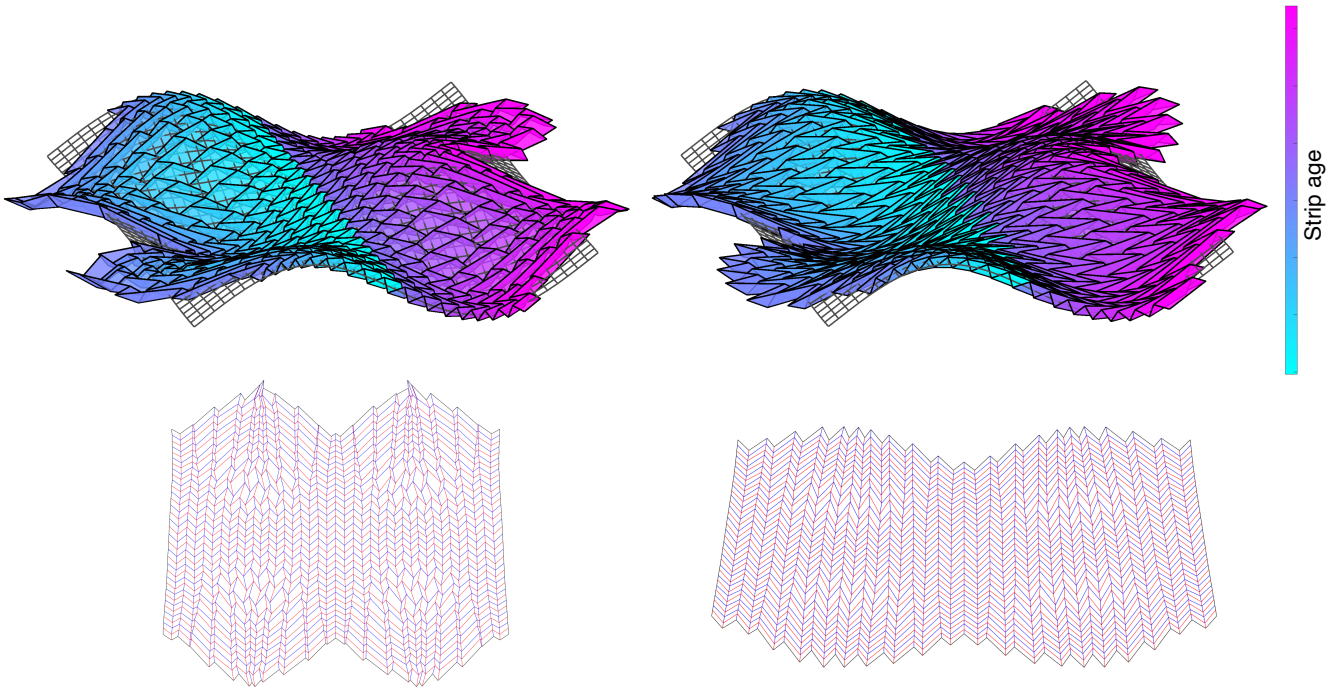

Fig. S12. Non-uniqueness of origami approximants for any given target surface. We use our additive framework to produce two surface-fitting origami structures with the same resolution approximating the same target surface. Here, the corrugation width of the seed strip of the right example is set to be twice of that of the left example. With the two different seed strips, it can be observed that both the 3D folded structures and the 2D crease patterns are significantly different.

where $\bar{\mathbf{r}}_i = (\mathbf{x}_i - \mathbf{y}_i)/\|\mathbf{x}_i - \mathbf{y}_i\|_2$, $\mathbf{x}_i$ is a point on the current growth front and $\mathbf{y}_i$ is its corresponding point on the previous growth front, to bound the flap angle optimization and thus avoid selecting trivial solutions.

In the closed loop growth pattern, boundary growth directions $\mathbf{r}_0$ and $\mathbf{r}_m$ overlap interior growth directions $\mathbf{r}_{m-1}$ and $\mathbf{r}_1$, respectively, and so we choose boundary design angles such that $\mathbf{r}_0 = \mathbf{r}_{m-1}$ and $\mathbf{r}_m = \mathbf{r}_1$.

Consider a set of planes parameterized by

$$\mathbf{X}(u, v) = u < \cos(j\phi), 0, \sin(j\phi) > +v < 0, 1, 0 > . \qquad [S36]$$

Edge lengths in the j^{th} new strip are given by the intersection of growth directions $\mathbf{r}$ and the plane $\mathbf{X}_d(u, v)$ displaced by d in the normal direction from $\mathbf{X}(u, v)$ where $d = (-1)^j h(1 + (j-1)\Delta h)/2$. The Huffman nested cones model in the main text (Fig. 4C) uses $\Delta h = 0.3$ and $\phi = \pi/18$. The twisted squares model in the main text (Fig. 4B) uses $\Delta h = 0$ and $\phi = \pi/180$.

A gallery of curved fold results created by our additive approach are presented in Fig. S14. It can be observed that our approach is capable of creating curved fold models with different geometry and topology. More specifically, note that each of the small constitutive folds in the model is a straight fold, as is necessary when working in a discrete setting. Nevertheless, by increasing the resolution of the folds, we can achieve models with folds resembling smooth curves.

C. Alternative curved fold model (main text Fig. 4D). In the Huffman example in the main text, we grow a curved fold surface by adding strips in the transverse direction to the curved folds (i.e. each growth front is a curved fold). In this example, we grow a curved fold surface by growing in the direction of the folds.

Consider a corrugated parabola given by

$$\mathbf{x}_i =< -1 + idx, (-1 + idx)^2 + dy(-1)^{i-1}, 0 >, \qquad [S37]$$

where $dx = 2/n$, $dy = .05$ and $i = 0, \ldots, n$. We use the corollary with $k_i = 1.04\pi$ to construct a strip of quads incident to $\mathbf{x}$.

We choose a flap angle of $\alpha_1 = 7\pi/8$ for every strip.

We choose boundary design angles such that the boundary growth directions $\mathbf{r}_0$ and $\mathbf{r}_m$ are parallel to their adjacent interior rays $\mathbf{r}_1$ and $\mathbf{r}_{m-1}$, respectively.

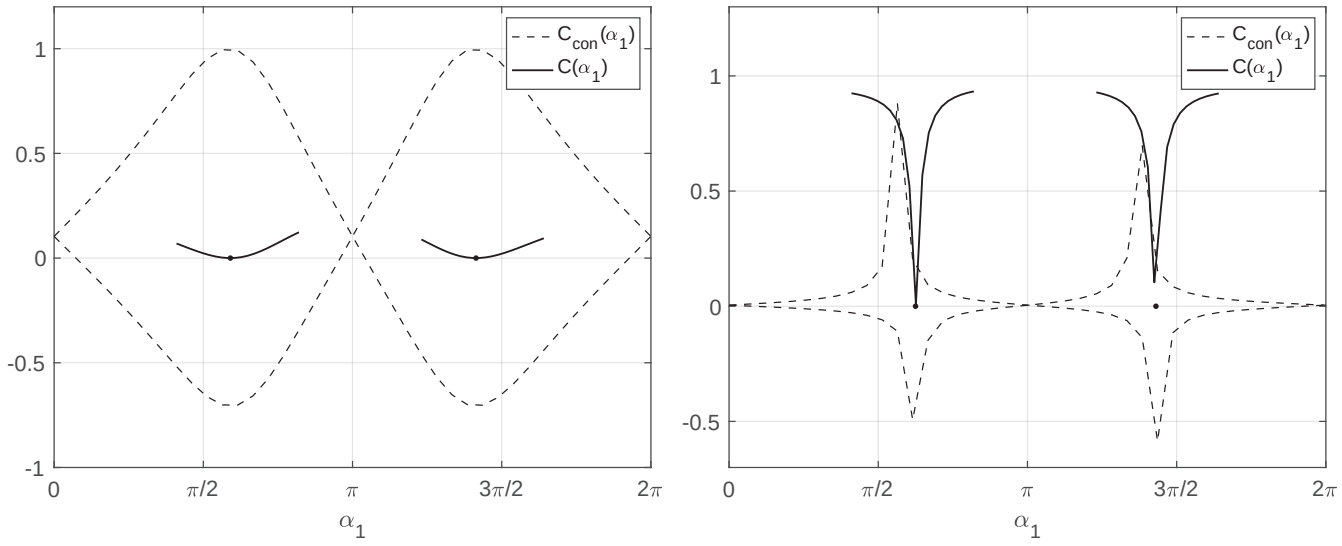

Fig. S13. Flap angle optimization for main text Figs. 4B,C. Dashed lines show the continuation cost function C_{con}, neighborhoods of whose minima give bounds for the optimization of cost function C (solid line), which gives the final flap angle choice (dot). **(Left)** Cost functions landscapes used to design the curved twist model from main text Fig. 4B. **(Right)** Cost functions landscapes used to design the curved twist model from main text main text Fig. 4C.

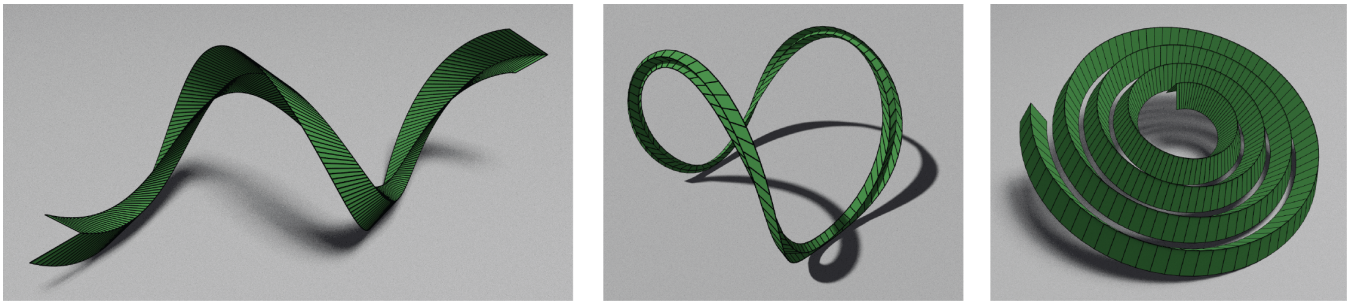

Fig. S14. Additional curved fold results. Using our additive approach, it is possible to create a wide range of curved fold models with different geometry and topology.

We choose all new new edge lengths to be $l_i = .1$.

D. Crumpled sheets (main text Fig. 4E). Finally, we deploy our strip construction to sample disordered, or "crumpled" folded sheets.

Consider three vectors

$$\mathbf{a} =< 0, \cos\nu, -\sin\nu >, \quad [S38]$$
$$\mathbf{b} =< 0, -\cos\nu, -\sin\nu >, \quad [S39]$$
$$\mathbf{c} =< -\sin\phi, 0, -\cos\phi >, \quad [S40]$$

with $\nu = \pi/2 - \beta/2$ and $\phi = \cos^{-1}(\cos((2\pi - k)/2)/\cos(\beta/2))$. Then the points

$$\bar{\mathbf{x}} = \{\mathbf{a}, \mathbf{0}, \mathbf{b}\} \quad [S41]$$
$$\bar{\mathbf{y}} = \{\mathbf{a} + \mathbf{c}, \mathbf{c}, \mathbf{b} + \mathbf{c}\} \quad [S42]$$

describe a pair of quads with growth front $\bar{\mathbf{x}}$ described by the familiar scalars β and k. This pair can be repeated in space by a shift of $\mathbf{b} - \mathbf{a}$ to form a Miura-like strip of quads given by two rows of points $\{\mathbf{x}'_i\}$ and $\{\mathbf{y}_i\}$ (with overlapping points deleted). To introduce disorder to the growth front, we perturb $\mathbf{x}_i$ with Gaussian noise according to

$$\mathbf{x}_i = (\mathbf{x}'_i - \mathbf{y}_\mathbf{i})(1 + X), \quad [S43]$$

where $X \sim \mathcal{N}(\mu = 0, \sigma = .4)$, which gives our final disordered seed with growth front $\mathbf{x}$. The seed from the disordered example in Fig. 4E in the main text consists of 20 quads and uses $\beta = 0.6\pi$ and $k = 1.2\pi$.

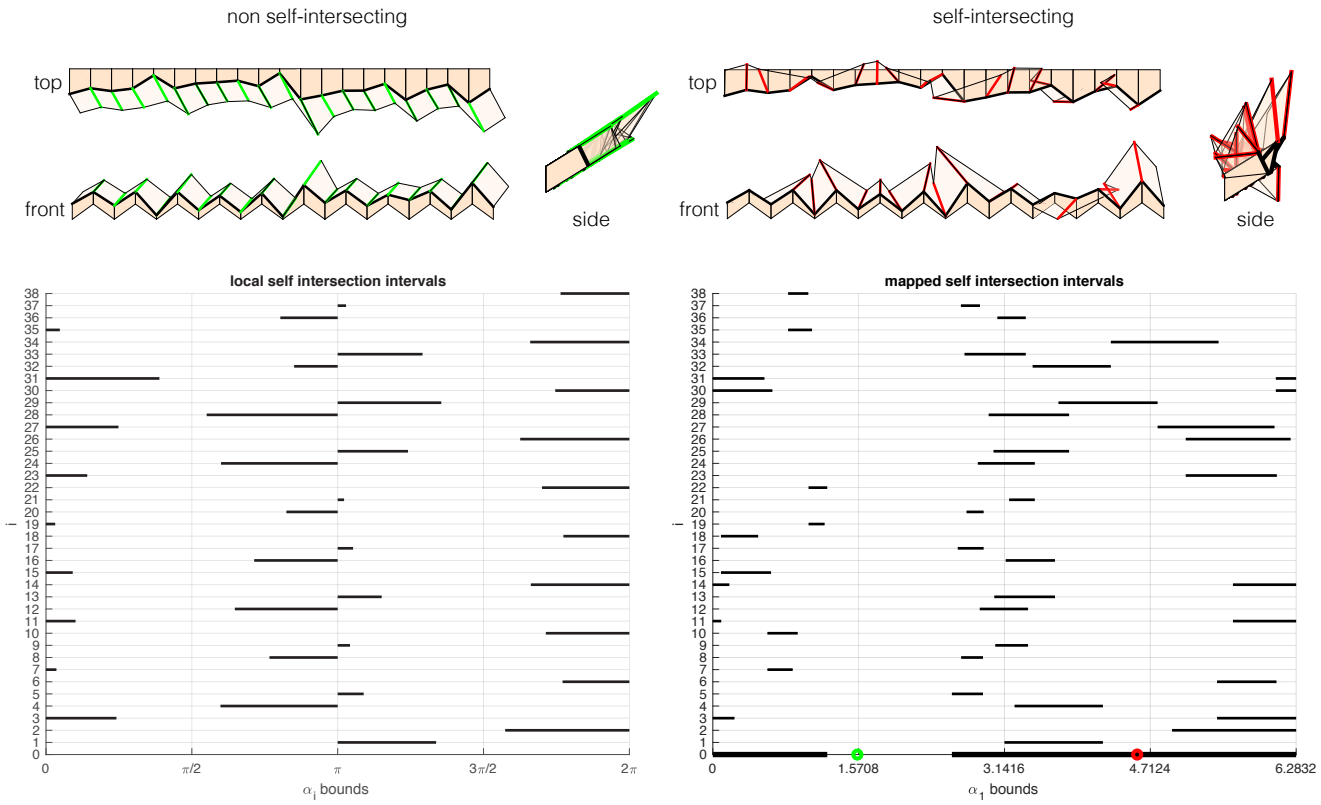

Fig. S15. Disordered strip self-intersection. (Top) A disordered strip with non self-intersecting (left) and self-intersecting flap angle choices **(Bottom)** Local (left) and mapped (right) self-intersection bounds corresponding to the above growth front. The union of all mapped intervals is shown in bold black at the bottom of the right plot, along with the flap angles values producing the above strip geometries.

Given the growth vertices $\mathbf{x}_i, i \in \{0, \ldots, m\}$, we compute intervals that give local self-intersection at each potential flap angle locations $i \in \{1, \ldots, m-1\}$ along the growth front (see Fig. S15). We can then use the inverse of g_i, the adjacent flap angle transfer function described in the main text, to map those local self-intersection intervals to a single growth front flap angle location. Let $g_i^{-1}(\alpha_{i+1}) = \alpha_i$ be given by

$$\alpha_i' = \text{mod}(\alpha_{i+1} + \phi_i, 2\pi) \quad [S44]$$

$$\theta_{i,2} = \text{mod}(\tan^{-1}((\cos(k_i) - \cos(\beta_i))/(\sin(\beta_i)\cos(\alpha_i') - \sin(k_i))), \pi) \quad [S45]$$

$$\theta_{i,1} = k_i - \theta_{i,2} \quad [S46]$$

$$\cos\alpha_i = (\cos(\theta_{i,2}) - \cos(\theta_{i,1})\cos(\beta_i))/(\sin(\theta_{i,1})\sin(\beta_i)) \quad [S47]$$

$$\sin\alpha_i = \sin(\theta_{i,2})/\sin(\theta_{i,1})\sin(\alpha_i') \quad [S48]$$

$$\alpha_i = \text{atan2}(\sin\alpha_i, \cos\alpha_i), \quad [S49]$$

then we map the $m-1$ intervals to the $m-2$ location, the mapped $m-1$ intervals and the $m-2$ intervals to the $m-3$ location and so forth until we have collected all local flap angle self-intersection intervals at the first flap angle α_1 location along the growth front. Once the local self-intersection intervals are mapped to a common flap angle location, we sample α_1 from the exterior of their union to give $\mathbf{r}_i, i \in \{1, \ldots, m-1\}$.

Boundary design angles are chosen such that the boundary growth directions $\mathbf{r}_0$ and $\mathbf{r}_m$ are parallel to their adjacent interior rays $\mathbf{r}_1$ and $\mathbf{r}_{m-1}$, respectively.

Define $L = \min(2, \min(\bar{l}_i))$, where $\bar{l}_i$ is the upper bound on the new edge length at growth front vertex $\mathbf{x}_i$. The edge length at location i is then sampled according to

$$l_i = X_i(1 - k_i/(2\pi))^p, i \in 1, \ldots, m-1, \quad [S50]$$

$$l_0 = X_i(1 - k_1/(2\pi))^p, \quad [S51]$$

$$l_m = X_i(1 - k_{m-1}/(2\pi))^p, \quad [S52]$$

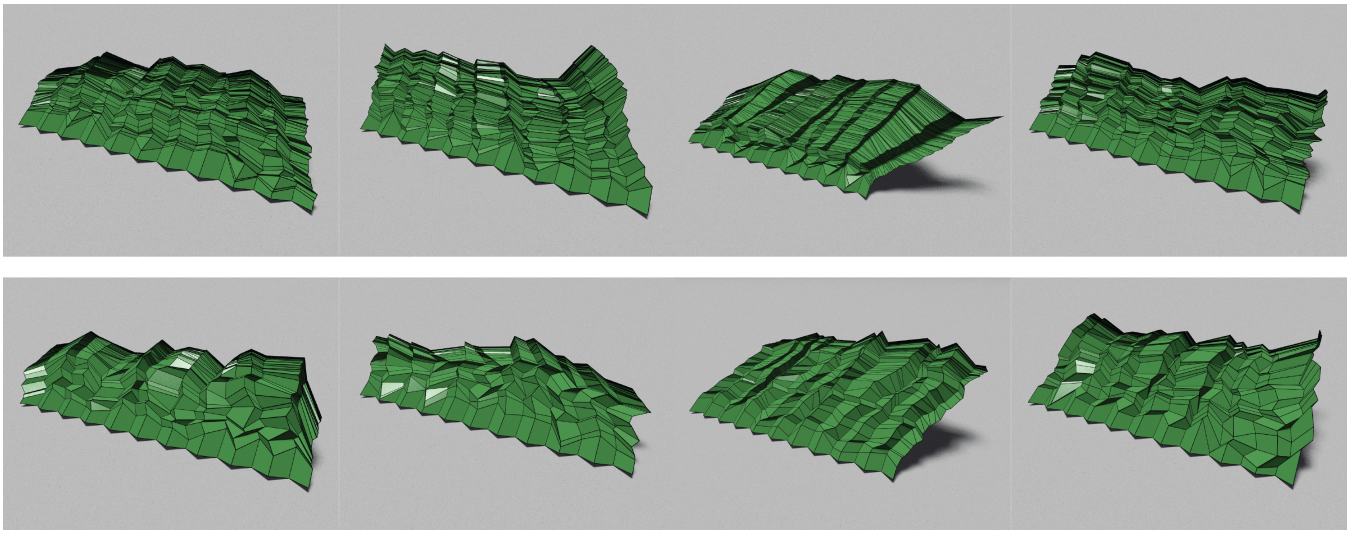

Fig. S16. Additional disordered results. The top row depicts other disordered examples using $p = 2$ and the bottom row examples use $p = 1$.

where $X_i \sim \mathcal{U}(0.1L, 0.9L)$. Intuitively, the scaling prefactor provides for a kind of anti-preferential attachment. Locations with large k_i (close to 2π) have highly convex developments and thus, at least locally, ample space to grow. Locations with small k_i (close to 0) have highly concave developments and thus, at least locally, restricted space to grow. The scaling prefactor, empirically, prevents caustics from forming and allows restricted locations to "catch up" with their relatively unrestricted counterparts by, somewhat counter-intuitively, encouraging growth in restricted locations and discouraging growth in unrestricted locations. The result in the main text uses $p = 2$. A gallery of other disordered results sampled in the same batch as that shown in the main text and a batch using $p = 1$ are presented in Fig. S16.

E. Brownian ribbon (main text Fig. 4F). To illustrate the flexibility of the corollary to our main theorem, we construct a set of folds that develop a Brownian path in $\mathbb{R}^3$ to a circle in $\mathbb{R}^2$. In this example, the growth front is no longer a front, but instead a curve in space not associated with an existing origami surface. This requires choosing the angular material k associated with the interior nodes of the target discrete curve in $\mathbb{R}^3$, rather than computing them from a the developability condition for an existing origami surface.

We sample a path $\mathbf{x}_i$ of Brownian motion with n steps in $\mathbb{R}^3$ according to

$$\mathbf{x}_i = \sum_{j=1}^{i} X_i, \tag{S53}$$

where $X \sim \mathcal{N}(\mu = 0, \sigma = 1)$ and $\mathbf{x}_0 =< 0, 0, 0 >$. The corollary allows us to inverse design the shape of the folding pattern up to the bounds $k_i \in (\beta_i, 2\pi - \beta_i)$, where β_i is the usual angle in space formed by the points $\mathbf{x}_{i-1}$, $\mathbf{x}_i$ and $\mathbf{x}_{i+1}$. Given a sampled path $\mathbf{x}$, we choose k according to

$$k_i = \cos^{-1}\left(\frac{\|\mathbf{e}_{i+1}\|_2}{2r}\right) + \cos^{-1}\left(\frac{\|\mathbf{e}_i\|_2}{2r_{\text{outer}}}\right), \tag{S54}$$

where r satisfies

$$\sum_{i=1}^{n} \sin^{-1}\left(\frac{\|\mathbf{e}_i\|_2}{2r_{\text{outer}}}\right) = \pi \tag{S55}$$

so that the development of $\mathbf{x}_i$ falls on a circle of radius r_{outer} and forms a closed loop. The result in the main text has $n = 400$ steps. To make visualization of the construction easier to follow, we show an example with $n = 10$ steps in Fig. S17.

We choose an arbitrary flap angle of $\alpha_1 = \pi/4$.

Boundary design angles are chosen according to

$$\theta_{0,2} = \cos^{-1}\left(\frac{\|\mathbf{e}_1\|_2}{2r_{\text{outer}}}\right) \tag{S56}$$

and

$$\theta_{n,1} = \cos^{-1}\left(\frac{\|\mathbf{e}_n\|_2}{2r_{\text{outer}}}\right), \tag{S57}$$

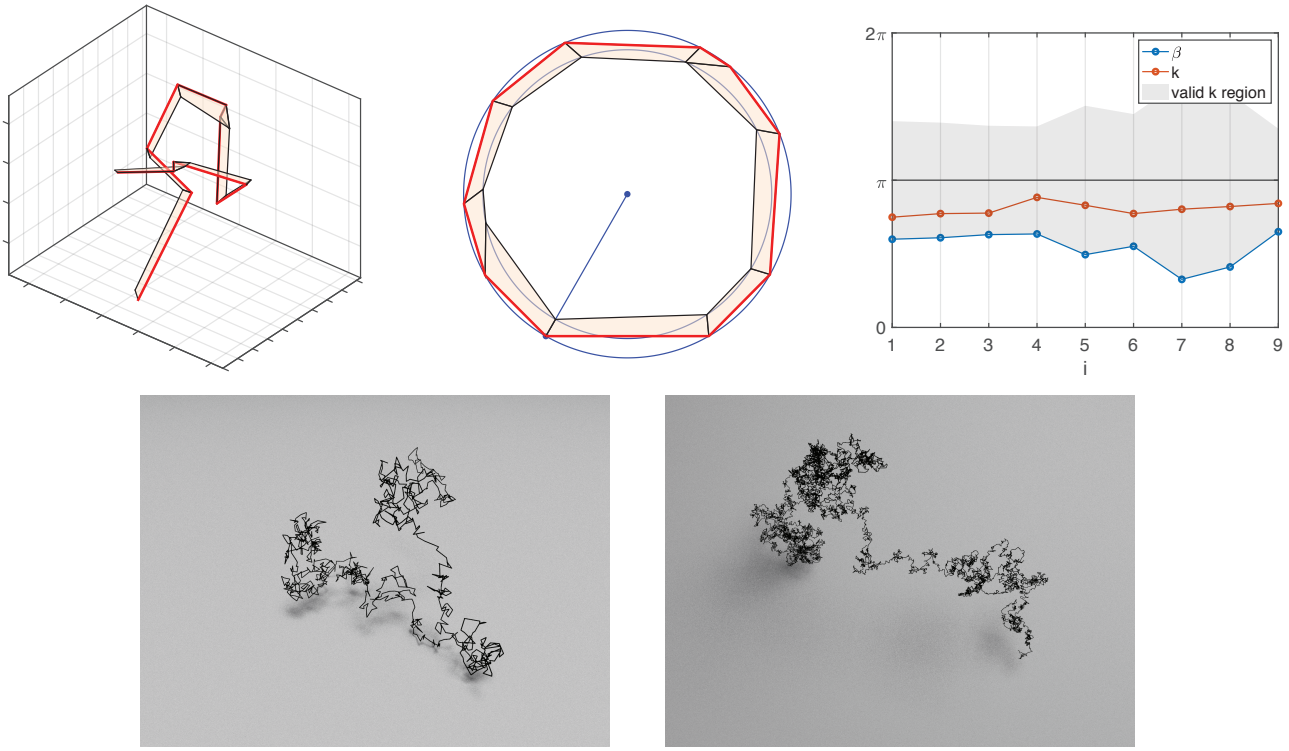

Fig. S17. Brownian ribbon. (Top Left) A strip of quads constructed by making use of the corollary to the main origami theorem in the main text pertaining to discrete curves. A Brownian path with 10 steps (red) is given as the seed. **(Top Middle)** By choosing appropriate values of k_i associated with the interior vertices of the Brownian path, the development of the strip of quads is designed such that the Brownian path maps to a circle of radius r_{outer} and the other side of the strip maps to a circle of radius r_{inner}. **(Top Right)** The values of β_i given (blue) and k_i chosen (red) at each interior vertex of the Brownian path, along with the bounds $(\beta_i, 2\pi - \beta_i)$ for the k_i choices. Different target planar shapes for the development of the Brownian path besides a circle could be designed by choosing different k_i within the valid region. **(Bottom Left)** Brownian ribbon with 1000 steps **(Bottom Right)** Brownian ribbon with 10000 steps

so that the developments of the growth directions $\mathbf{r}_0$ and $\mathbf{r}_m$ are equal and fall on the line containing the development of $\mathbf{x}_0$ (which is equal to the development of $\mathbf{x}_n$) and the origin of the pattern's circumscribed circle.

Edge lengths l_i are chosen such that the points on the other side of the developed ribbon fall on a circle of smaller radius than r_{inner} with the same origin:

$$\theta_{i,r} = \cos^{-1}\left(\frac{-\mathbf{e}_i \cdot \mathbf{r}_i}{\|\mathbf{e}_i\|_2 \|\mathbf{r}_i\|_2}\right) - \cos^{-1}\left(\frac{\|\mathbf{e}_i\|_2}{2r_{\text{outer}}}\right), \quad [S58]$$

$$l_i = r_{\text{outer}} \cos\theta_{i,r} - \sqrt{r_{\text{inner}}^2 - r_{\text{outer}}^2 \sin^2\theta_{i,r}}. \quad [S59]$$

The above expression is valid when $r_{\text{inner}}/r_{\text{outer}} > \sin\theta_{i,r}$, where $\theta_{i,r}$ is the angle the development of $\mathbf{r}_i$ makes with the radial direction.

S5. Folding simulation

As all models generated by our additive framework are developable, there is always an elastic folding process that allows them to transform from a 2D flat sheet to a 3D structure, possibly with geometrical frustration at the intermediate states (as the models are not necessarily rigid-foldable). To show this, we apply the fast, interactive origami simulator (3) available online (4) to simulate the folding process of our models. More specifically, for each model, we provide the 2D crease pattern and the target fold angle for each edge in the final 3D structure as the inputs for the simulator, which then folds every crease simultaneously using a compliant dynamic simulation method, using reasonable (default) simulation settings (numerical integration scheme = Euler (first order), axial stiffness = 20, face stiffness = 0.2, fold stiffness = 0.7, facet crease stiffness = 0.7, damping ratio = 0.45). Fig. S18 shows the snapshots of the folding simulation for several models created by our framework, and Video S10 shows an animation of one of them.

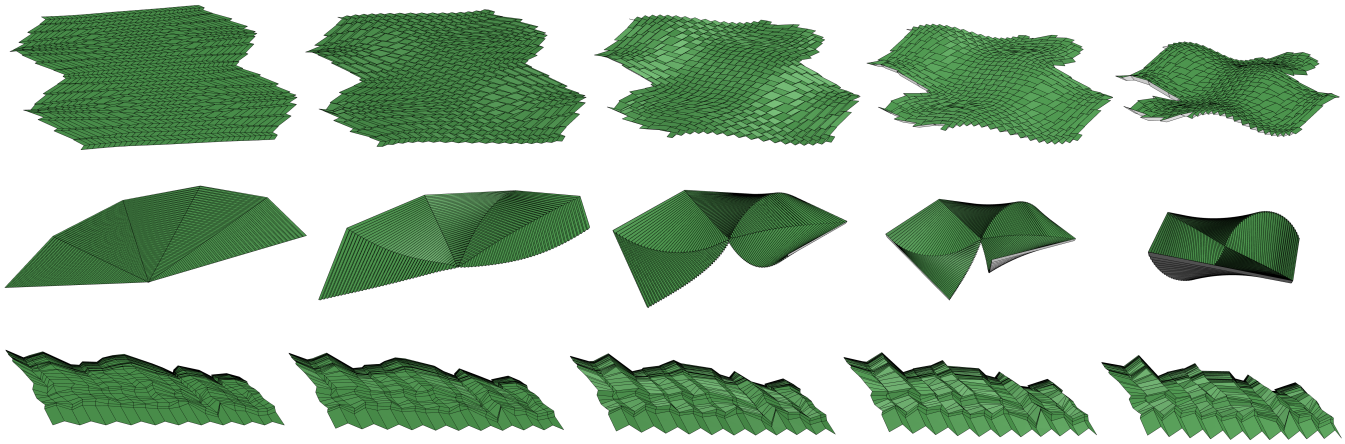

Fig. S18. Folding simulation. Each row shows the simulated folding process of a model obtained by our additive framework, from the 2D flat state (leftmost) to the final 3D folded structure (rightmost).

S6. Description of supplementary videos

Movie S1. An animation of the single and adjacent vertex origami in Fig. 1 in the main text.

Given two boundary design angles $\theta_{i,3}, \theta_{i,4}$ (blue) and the angle in space between the two existing quads (green), we can freely choose the flap angle α_i (red). These angles together uniquely determine the new design angles $\theta_{i,1}$ (yellow) and $\theta_{i,2}$ (dashed) by the local developability constraint. In other words, α_i parameterizes the ellipse γ_i of spherical arcs $\theta_{i,1}, \theta_{i,2}$ which forms a closed loop around the line containing $\mathbf{e}_i$. The choice of α_i does not only determine the geometry of the single vertex origami but also propagates to all other vertices at the growth front via adjacency.

- **00:00-00:09** Flap angle α_i (red) rotates a half-plane about growth front edge $\mathbf{e}_i$ incident to growth front vertex $\mathbf{x}_i$.
- **00:09-00:20** The first new design angle $\theta_{i,1}$ moves in the plane determined by α_i and intersects γ_i uniquely, determining $\mathbf{r}_i$, $\theta_{i,1}$ and $\theta_{i,2}$ for a given α_i.
- **00:20-00:28** α_i parameterizes γ_i uniquely: for every choice of α_i there is a unique growth direction $\mathbf{r}_i$.
- **00:28-00:33** Rotating 3D view of single vertex system at growth front vertex $\mathbf{x}_i$.
- **00:33-00:46** An adjacent growth front vertex $\mathbf{x}_{i+1}$ is introduced. Flap angle α_{i+1} of this new vertex is determined by the choice of the preceding flap angle α_i, giving the half-plane of action for the new design θ_{i+1}, which intersects γ_{i+1} uniquely.
- **00:46-00:54** This is true for every α_i, so α_i parameterizes γ_{i+1} and adjacent growth direction $\mathbf{r}_{i+1}$ and design angles $\theta_{i+1,1}$ and $\theta_{i+1,2}$ are determined by α_i.
- **00:54-00:58** Rotating 3D view of adjacent vertex system at growth front vertices $\mathbf{x}_i$ and $\mathbf{x}_{i+1}$.

Movie S2. An animation illustrating the choice of the flap angle for a pair of folded quads in Fig. 3A and B in the main text.

- **00:00-00:10** Sweeping flap angle α through $[0, 2\pi)$ gives the range of single vertex origami models possible at a growth front vertex (left). Mountain-valley patterns (top left) and values of new design angle θ_1 are shown for each flap angle value scanned.
- **00:10-00:16** Special vertex solution given by $\alpha = 0$ is shown rotating in 3D. This flap angle gives a trivially locked configuration with coplanar θ_1 and θ_2 faces.
- **00:19-00:21** Flat-foldable $\theta_1 + \theta_3 = \theta_2 + \theta_4 = \pi$ special vertex solution given by α_{ff}
- **00:22-00:24** Equal new design angles ($\theta_1 = \theta_2$) special vertex solution given by α_{eq}
- **00:24-00:30** Special vertex continuation solution given by α_{con} is shown rotating in 3D. This flap angle continues the existing fold on the interior of the growth front, giving a single vertex origami with no new folds and coplanar θ_1 and θ_4 faces and θ_2 and θ_3 faces.

- **00:31-00:37** Special vertex solution given by $\alpha = \pi$ is shown rotating in 3D. This flap angle gives a trivially locked configuration with coplanar θ_1 and θ_2 faces.
- **00:37-00:38** Flap angle scans through the interval $\alpha \in (\pi, \alpha_{\text{lr}})$ producing self-intersecting single vertex origami.
- **00:38-00:44** Special vertex locked-right solution given by α_{lr} is shown rotating in 3D. This flap angle gives a locked single vertex origami with coplanar θ_1 and θ_4 faces.
- **00:45-00:51** Second special vertex continuation solution, given by reflection of the first α_{con} over the β plane, is shown rotating in 3D. This flap angle produces the same design angles as the first α_{con} but embeds them in space such that new folds are created.
- **00:51-00:53** Second equal new design angles ($\theta_1 = \theta_2$) special vertex solution given by reflection of the first α_{eq} over the β plane
- **00:54-00:56** Second flat-foldable $\theta_1 + \theta_3 = \theta_2 + \theta_4 = \pi$ special vertex solution given by reflection of the first α_{ff} over the β plane
- **00:57-01:03** Special vertex locked-left solution given by α_{ll} is shown rotating in 3D. This flap angle gives a locked single vertex origami with coplanar θ_2 and θ_3 faces.
- **01:03-01:05** Flap angle scans through the interval $\alpha \in (\alpha_{\text{ll}}, 2\pi)$ producing self-intersecting single vertex origami.
- **01:05-01:07** The single-vertex origami transitions to illustrate the effect the pair of scalars β, the green angle in space along the growth front, and k, the amount of angular material needed to construct the two new design angles and the shape parameter of γ, have in characterizing the design space of a single vertex origami. A plot of the valid region of these scalars corresponding to the plane of the plot in Fig. 3B is shown on the right, with a black circle at the point in this region depicted on the left.
- **01:07-01:17** For a given β, varying $k \in (\beta, 2\pi - \beta)$ changes the shape of γ, i.e. the space of new growth directions $\mathbf{r}$. As k approaches β, γ collapses to the arc swept out by β in space. As k approaches $2\pi - \beta$, γ collapses to the another arc measuring β in space given by extending the growth front edges through $\mathbf{x}$.
- **01:17-01:27** For a given k, varying $\beta \in (0, \pi - |\pi - k|)$ changes the angle of the growth front in space. As k approaches 0, γ approaches a simple cone shape with the colinear growth front edges as its axis. As k approaches $\pi - |\pi - k|$, collapses to an arc measuring β in space.
- **01:27-01:38** Both β and k vary to trace a path in the valid region that visits the red, green and blue points identified in Fig. 3B.

Movie S3. An animation illustrating the choice of the flap angle for a quad strip in Fig. 3C in the main text.

Given a folded quad strip, changing the flap angle α_1 of the first new face produces a wide range of compatible growth directions for the new strip (top). The new interior design angles $\theta_{i,1}$ in the new strip, fold angles transverse to the growth front $\phi_{i,\text{t}}$ and parallel to the growth front $\phi_{i,\text{p}}$ all vary as a function of the flap angle α_1 (bottom right). Boundary growth directions and edge lengths are chosen arbitrarily. The corresponding mountain-valley pattern is also shown (bottom left).

- **00:03-00:11** The new strip geometry given by $\alpha_{1,\text{con}}$ has no new folds.
- **00:14-00:22** The new strip geometry given by $\alpha_{1,\text{fold}}$ has new, non-trivial folds along the growth front and in the new strip.

Movie S4. An animation of the surface fitting model in Fig. 4A in the main text.

Movie S5. An animation of the twisted squares model in Fig. 4B in the main text.

Movie S6. An animation of the Huffman nested cones model in Fig. 4C in the main text.

Movie S7. An animation of the curved fold model in Fig. 4D in the main text.

Movie S8. An animation of the disordered model in Fig. 4E in the main text.

Movie S9. An animation of the Brownian fold model in Fig. 4F in the main text.

Movie S10. A simulation of the folding process for a surface fitting model obtained by our additive approach.

References

1. LH Dudte, E Vouga, T Tachi, L Mahadevan, Programming curvature using origami tessellations. *Nat. Mater.* **15**, 583–588 (2016).
2. T Kawasaki, On the relation between mountain-creases and valley-creases of a flat origami in *Proceedings of the First International Meeting of Origami Science and Technology.* pp. 229–237 (1991).
3. A Ghassaei, ED Demaine, N Gershenfeld, Fast, interactive origami simulation using GPU computation in *Origami^7: Proceedings of the 7th International Meeting on Origami in Science, Mathematics and Education (OSME 2018)*. Vol. 4, pp. 1151–1166 (2018).
4. A Ghassaei, ED Demaine, N Gershenfeld, Origami simulator (https://origamisimulator.org/) (2018).